

## Research



**Cite this article:** Jamin T, Gordillo L, Ruiz-Chavarría G, Berhanu M, Falcon E. 2015 Experiments on generation of surface waves by an underwater moving bottom. *Proc. R. Soc. A* **471**: 20150069. <http://dx.doi.org/10.1098/rspa.2015.0069>

Received: 2 February 2015

Accepted: 30 April 2015

### Subject Areas:

fluid mechanics, wave motion, geophysics

### Keywords:

tsunami generation, gravity surface waves, linearized water wave problem

### Author for correspondence:

Leonardo Gordillo  
e-mail: [lgordill@ing.uchile.cl](mailto:lgordill@ing.uchile.cl)

Electronic supplementary material is available at <http://dx.doi.org/10.1098/rspa.2015.0069> or via <http://rspa.royalsocietypublishing.org>.

# Experiments on generation of surface waves by an underwater moving bottom

Timothée Jamin<sup>1</sup>, Leonardo Gordillo<sup>1,3</sup>, Gerardo Ruiz-Chavarría<sup>2</sup>, Michael Berhanu<sup>1</sup> and Eric Falcon<sup>1</sup>

<sup>1</sup>Université Paris Diderot, Sorbonne Paris Cité, MSC, UMR 7057 CNRS, 75013 Paris, France

<sup>2</sup>Facultad de Ciencias, Universidad Nacional Autónoma de México, 04510 México DF, Mexico

<sup>3</sup>Departamento de Física, Facultad de Ciencias Físicas y Matemáticas, Universidad de Chile, Casilla 487-3, Santiago, Chile

 LG, 0000-0002-9516-1346

We report laboratory experiments on surface waves generated in a uniform fluid layer whose bottom undergoes an upward motion. Simultaneous measurements of the free-surface deformation and the fluid velocity field are focused on the role of the bottom kinematics (i.e. its spatio-temporal features) in wave generation. We observe that the fluid layer transfers bottom motion to the free surface as a temporal high-pass filter coupled with a spatial low-pass filter. Both filter effects are often neglected in tsunami warning systems, particularly in real-time forecast. Our results display good agreement with a prevailing linear theory without any parameter fitting. Based on our experimental findings, we provide a simple theoretical approach for modelling the rapid kinematics limit that is applicable even for initially non-flat bottoms: this may be a key step for more realistic varying bathymetry in tsunami scenarios.

## 1. Introduction

Most tsunamis are triggered by sudden displacements of the seabed during earthquakes. To predict tsunami hazards in real time, actual warning models require, first and foremost, data of the free-surface initial waveform in the open seas. Buoy networks dedicated to detect tsunamis may provide direct measurements of wave heights at fixed positions across the oceans [1], which can be used to reconstruct the initial tsunami waveform

through inversion. However, these data only become available after the tsunami waves have reached the buoy locations. As reconstruction comes from inversion, data are not only required in a single buoy but in a set of them, which means that waveform estimations become reliable only after tsunamis have travelled an important distance across the sea. Far-field locations can thus rely on buoy network data, but not near-field locations, which are usually struck by the tsunami waves before the initial waveform can be reconstructed.

Tsunami warning systems thus require an alternative way to estimate the tsunami initial waveform while buoy records are unavailable. The standard is to use a faster indirect method based on the fault source and the seismic data from nearby stations. The seabed displacement is computed numerically from the fault slip parameters using Okada's model [2], and then translated to the ocean free surface. The technique provides a fast estimation of the initial waveform that can be used as an input for tsunami-propagation codes. Tsunami risks at different locations can then be forecasted using a discretized version of the estimated waveform via ready-to-use *offline* calculations (Green's functions) [3]. However, this procedure often underestimates the surface wave amplitude (e.g. for the 2004 Indian Ocean tsunami [4]).

Several reasons have been proposed to explain this bias [5–12], including the seabed-kinematics role during an earthquake (i.e. its spatio-temporal features) [12–15]. Bottom displacement is considered to be instantaneous if its typical rise time is small compared with the time scale of the generated waves at the free surface [14]. Most earthquakes meet this condition, although other remarkable tsunamigenic events barely satisfy it: for instance, in two of the largest tsunamis ever registered, the bottom displacements may have been notably slow [16]. Numerical codes used in warning systems, however, are more focused on analysing wave propagation on the varying bathymetry of oceanic basins, which is achieved via numerical integration of nonlinear shallow water equations (e.g. the MOST [17] and the TUNAMI [18]). Warning codes are prone to neglect seabed kinematics and consider that bottom displacements are instantaneous. Thus, they use as initial condition a simple translation of the final deformation of the source bottom to the ocean surface. On the other hand, numerical simulations that do suitably consider bed-sea kinematic coupling during displacements are at hand and in a broad range of approaches: linear three-dimensional (3D) potential flow [19], higher order nonlinear shallow-water theory [20], fully nonlinear potential flow [21,22] and full Navier–Stokes equations [23,24] (for a comparison between several approaches, see [25]). Computational costs however remain high in most cases, which makes their application for real-time forecasting hard. Furthermore, numerical simulations also require bottom kinematics *a priori*, an input that is hard to determine during events. During the last few years, a powerful non-hydrostatic numerical model, NHWAVE have come into scene [26]. The model is able to predict 3D effects for a given initial condition (i.e. initially non-flat bottom) with an outstanding accuracy and lower computational cost by splitting the ocean in very few vertical layers. Results are very promising [27].

Numerical simulations, theory and experiments show that bottom dynamics play a role. Even if the deformation happens at the instantaneous limit, the free-surface displacement is not equal to the bottom one as considered by translational models [28–30]. In realistic scenarios, hindcast simulations have also shown that bed dynamics do have an effect. For the 2011 Tohoku tsunami, Grilli *et al.* [27] showed using both NHWAVE and high-order Boussinesq simulations that dynamic-source models yield tsunami waveforms remarkably different than instantaneous source models. Indeed, dynamic models show an excellent agreement with field measurements.

On the other hand, laboratory experiments dealing with the influence of bed-uplift kinematics in tsunami generation are rare and have been based on measurements of the free-surface deformation [29,31–33], providing limited information about the fluid dynamics. Velocity measurements in the bulk are even rarer and only concern landslide-triggered tsunamis [34,35]. Furthermore, most of these laboratory experiments have been performed in channels overlooking the 3D geometry of real scenarios [29,32,34–36]. The lack of tsunami-oriented experiments contrasts with their unquestionable importance. Controlled laboratory experiments not only supply a way to validate numerical simulations under well-known inputs (cf. [37]), but also may elucidate which physical mechanisms dominate a given regime.

In this article, we analyse experimentally and theoretically the hydrodynamic coupling between the bottom and the free-surface motion in a 3D fluid layer, focusing on the role that the bottom kinematics play in wave generation. We aim to better understand how spatio-temporal features of the bottom deformation affect the shape and the amplitude of the generated waves. For this purpose, we designed an idealized scenario where waves are generated by an axisymmetric deformation in the centre of a flat-bottom laboratory tank. We performed combined measurements of the free-surface deformation and the fluid velocity field. Our results are then compared with a linear theory for underwater moving bottoms [38]. Although some of our experimental parameters are by orders of magnitude far from real tsunami-generation conditions, essential features are still well reproduced. Based on our experimental findings, we also provide a theoretical framework that gives a simple and different insight on the generation of waves by impulsive bottom motions. The results could be applied to determine initial waveforms in uneven bottom configurations.

## 2. Experimental set-up

We performed our experiments in a  $110 \times 110 \times 30 \text{ cm}^3$  Plexiglas basin filled with water to a depth of  $h = 2.5 \text{ cm}$ . A circular region (radius  $r_2 = 3.25 \text{ cm}$ ) was carved in the bottom centre and covered with a stretched elastic sheet. The sheet is deformed by means of a solid flat circular piston ( $r_1 = 2.5 \text{ cm}$ ) placed beneath the membrane and attached to an electromechanical shaker (figure 1). As a result of the set-up geometry, the bottom vertical motion can be described as a separable spatio-temporal function with circular symmetry,  $\zeta(r, t) = \zeta_m \alpha(r) \beta(t)$ , where  $\zeta_m$  is the maximal bottom deformation;  $\alpha(r)$  is the spatial profile along the radial horizontal coordinate  $r$  (figure 1 (inset)); and  $\beta(t)$  is the displacement time function. The last one was arbitrarily chosen to be an exponential rise,  $\beta_{\text{exp}}(t) = 1 - e^{-t/\tau_b}$ , or a half-sine one,  $\beta_{\text{sin}}(t) = \sin^2[\pi t/(2\tau_b)]$  if  $t \leq \tau_b$  or 1 if  $t > \tau_b$ ; where  $\tau_b$  is defined as the rise time. To achieve this, the shaker input signal was determined by exploiting the bottom velocity records from a laser Doppler vibrometer. Our system can be used to study several rise times, and upward bottom amplitudes. Value ranges are displayed in the following table:

bed displacement function	$\tau_b$	$\zeta_m$
exponential $\beta_{\text{exp}}(t)$	10 – 500 ms	1.5 – 5.0 mm
half-sinus $\beta_{\text{sin}}(t)$	10 – 500 ms	1.5 – 5.0 mm

Thus, typical bottom velocities vary from 1 to  $30 \text{ cm s}^{-1}$ . A total number of 22 different scenarios (different bed displacement function,  $\tau_b$  and  $\zeta_m$ ), each consisting of 10 runs, were analysed. The basin extent was chosen to avoid wave reflections on the lateral walls during the generation process.

The velocity field in the bulk during bottom and surface deformations is obtained using Particle Image Velocimetry (PIV). A laser sheet passing through the basin centre illuminated a vertical slice of water seeded with  $50 \mu\text{m}$  polyamide particles (PSP), as shown in figure 1. To avoid particle settling, the water was mixed with some NaCl (up to a mass concentration of 2.7%) so the aqueous solution matches the density of particles. A high-speed camera placed in front of the illuminated region provided an imaging area of  $71 \times 30 \text{ mm}^2$  ( $1600 \times 692$  pixels), which was recorded at 500 Hz during  $\tau_m = 1 \text{ s}$  ( $\tau_m$  is defined as the measurement time). Since the system is axisymmetric, these measurements build a 3D picture of the flow. The surface of the water layer was blown with more particles, which due to their surface tension, tend to rest in the surface. In the images, the particles form an identifiable line, which can be used for detection (figure 2). The free-surface vertical deformation  $\eta(r, t)$  was then obtained by applying a Radon transform algorithm on the images [39]. This algorithm integrates the intensity along all the possible straight lines contained in a sub-window and finds the maximal value. A continuous and smooth curve is then obtained by interpolating the segments (slope and position) along the whole free surface. An example of the detected free surface by the algorithm is plotted in figure 2. Finally, we applied

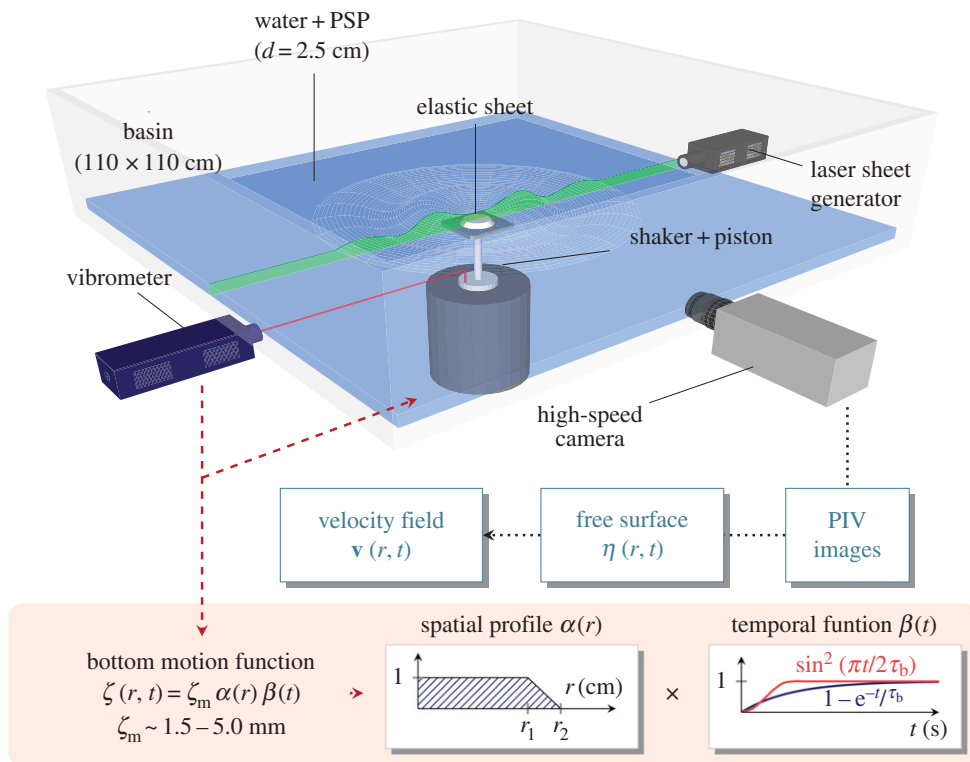


**Figure 1.** Experimental set-up. A layer of water is contained in a basin where a shaker-piston vertically deforms an elastic sheet placed at the bottom centre. The piston motion is recorded using a laser vibrometer. Images from a sectional cut of the fluid are obtained using a laser sheet generator and a high-speed camera. The bottom dimensionless spatial profile  $\alpha(r)$  and the time displacement function  $\beta(t)$  are also displayed. (Online version in colour.)

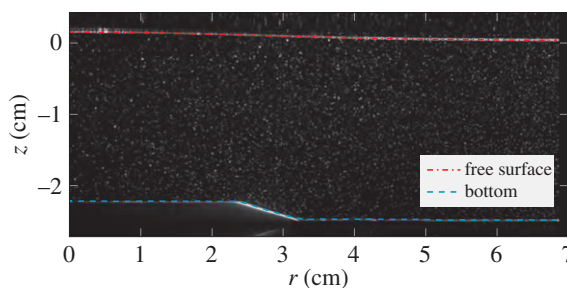


**Figure 2.** A typical image of the region of interest (side view) for the study of waves generated by a moving bottom. The liquid is seeded with particles (white points) both in the bulk and in the free surface. Those at the free surface form a quasi-continuous brighter line that is used to identify the position of the free surface  $\eta(r, t)$ . The bottom position  $\zeta(r, t)$  can also be detected with standard contrast techniques. The snapshot was taken at  $t = 80$  ms in a half-sinus bed deformation scenario ( $\zeta_m = 5$  mm,  $\tau_b = 150$  ms,  $h = 2.5$  cm). (Online version in colour.)

a PIV grid-refining scheme [40] (up to  $16 \times 16$  pixels windows, no overlapping) using an average correlation method [41] on 10 experimental runs for each set of parameters.<sup>1</sup> All the data used throughout this article are available at a public repository at [42].

The two time scales in our experiment are the bottom rise time  $\tau_b$  and the typical time of the generated waves  $\tau_w$ . We defined  $\tau_w$  as the semi-period of the wave, i.e. the time between

<sup>1</sup>Owing to the reproducibility of experiments, we superimpose pictures of 10 identical runs to increase the number of particles on the processed images, improving PIV results.

the first maximum and minimum of the water surface deformation at the basin centre ( $r = 0$ ). In our experiment,  $\tau_w \simeq 130$  ms is the same for any displacement time function  $\beta$  and most of rise times  $\tau_b$  (see results below). This value is related to the dominant wavelength of the generated wave  $\lambda_w \approx 10$  cm (according to acquired images), through the dispersion relation  $\tau_w = \pi / \sqrt{gk_w \tanh k_w h}$ , where  $g$  is gravity and  $k_w$  is the dominant wavenumber of the generated wave.<sup>2</sup> Note that  $\lambda_w > 2r_2 = 6.5$  cm. During measurements, capillary waves were not observed<sup>3</sup> (see discussion in §3c). We focus on one experimental time ratio simply defined as  $\bar{\tau} = \tau_b / \tau_w$ , which varies between 0.08 and 4. The relevance of the time ratio in tsunami generation was noticed by Hammack [29], who suitably identified three wave-response regimes to bottom deformations: impulsive ( $\bar{\tau} \ll 1$ ), transitional ( $\bar{\tau} \sim 1$ ) and creeping ones ( $\bar{\tau} \gg 1$ ). The Froude number in our measurements  $Fr = \zeta_m / \tau_b \sqrt{g h}$  varies between 0.02 and 0.3.

### 3. Results and discussion

#### (a) Velocity field

Within the above classification, we display (in figure 3) three characteristic snapshots of the wave-generation velocity fields for half-sine type displacements. The vertical coordinate is denoted as  $z$  such that at rest, the free surface matches  $z = 0$  and the bottom,  $z = -h$ . When  $\bar{\tau} \ll 1$ , we observe an upward global motion during the bottom uplift. Indeed, the velocity field just below the free surface is vertical (figure 3a) as predicted in [43]. Gravity-wave propagation starts remarkably after the end of the bottom motion as shown in videos.<sup>4</sup> When  $\bar{\tau} \sim 1$ , the flow resembles that of figure 3a at short times. However, before the bottom motion ends, waves start to propagate radially from the generation region: an oscillating flow occurs right beneath the free surface (figure 3b). In this case, both bottom deformation and wave propagation occur simultaneously suggesting that the bottom kinematics affects induced waves. For  $\bar{\tau} \gg 1$ , the free surface remains mostly stationary and accordingly, the vertical component of the velocity vanishes when approaching the free surface (figure 3c). In this stage, the outward flow reminds that of a moving bottom in the presence of a fixed boundary at  $z = 0$ . We observed that exponential-rise bottom displacements (not shown) display similar behaviour.

To quantify the transition between the slow and rapid regimes, we compute the kinetic energy from the fluid velocity field. Figure 3 shows that the region  $r < 7$  cm contains most of the kinetic energy during the bottom deformation. As shown in figure 4 (inset), the kinetic energy within this volume,  $E_K$ , captures also the main temporal features of the motion (see also [44]). The bottom uplift induces an intense first maximum of  $E_K$ . As the bottom stops afterwards, a local minimum  $E_K^-$  appears and later, a second maximum  $E_K^+$  emerges induced by wave propagation. We define the contrast of kinetic energy as  $(E_K^+ - E_K^-) / (E_K^+ + E_K^-)$ . As shown in figure 4, the contrast is close to unity for  $\bar{\tau} \ll 1$ : the liquid can be considered as motionless at the end of the bottom deformation ( $E_K^- \approx 0$ ), with its velocity being negligible compared with those due to wave propagation. Inertia seems to be absent since no flow outlasts the bottom motion: the liquid layer and the bottom behaves like a single block. For larger  $\bar{\tau}$ , the wave propagation begins while the bottom is still moving so the energy contrast decreases to zero. Furthermore, for  $\bar{\tau} \gtrsim 1.4$ , the contrast is not defined any more because the bottom deformation and the wave propagation overlap so much that  $E_K^-$  and  $E_K^+$  do not exist at all. This shows that the energy contrast depicts well the transition between rapid and slow scenarios. The data scattering observed in figure 4 has no physical origin and is inherent to PIV measurements as the technique holds some uncertainties. For exponential

<sup>2</sup>The generated wave is mainly dispersive as  $\lambda_w = 4h$ , in contrast with real tsunami scenarios where waves are less dispersive.

<sup>3</sup>The electromechanical shaker was intentionally decoupled from the tank (no solid contact) so that high-frequency vibrations could not be directly transferred to the tank. The only contact took place between the piston and the soft membrane used for the bottom deformation. This configuration avoids the emergence of capillary waves due to shocks at small  $\tau_b$  bed uprise motion. Notice that PSP particles at the free surface are likely to inhibit capillary waves.

<sup>4</sup>See the electronic supplementary material for velocity-field videos of the runs depicted in figure 3.



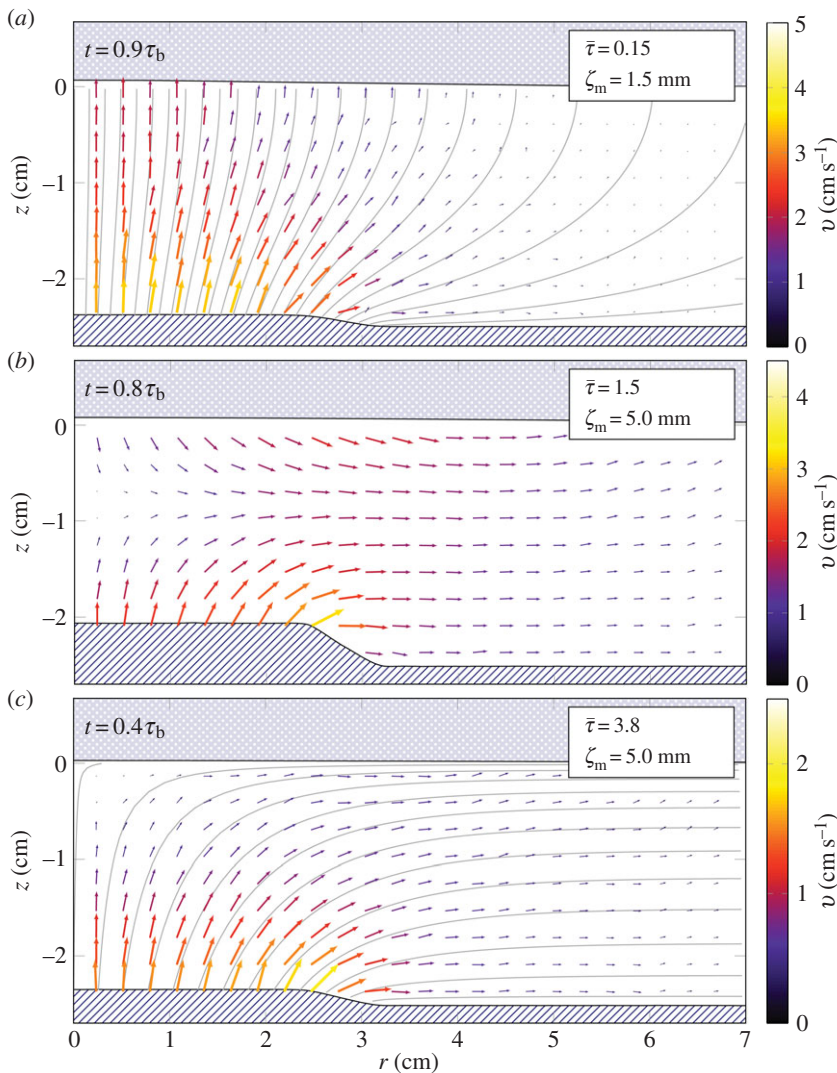


**Figure 3.** Experimental velocity fields in the water during half-sine bottom displacements for three typical  $\bar{\tau}$  values. The streamlines (set of grey curves) in (a,c) were computed numerically using an asymptotic model for the  $\bar{\tau} \ll 1$  and  $\bar{\tau} \gg 1$  cases (see explanation in §3d). In all cases, the free-surface deformation is significantly smoother than the bottom one. (Online version in colour.)

bottom motions (not shown), times at which extrema of  $E_K$  occur are different from the half-sine case,<sup>5</sup> but the contrast of kinetic energy behaves similarly with  $\bar{\tau}$ .

## (b) Free surface

Since the fluid velocity field is coupled with the free-surface deformation, both quantities share related spatio-temporal features.<sup>6</sup> The insets of figure 5 depict the bottom and the free-surface elevations at  $r=0$ ,  $\zeta_0(t)$  and  $\eta_0(t)$ , as a function of time. We observe in all cases that the free surface and the bottom are synchronized at the beginning of the motion. For  $\bar{\tau} \ll 1$ , this is true throughout the bottom uplift and regardless of the displacement time function  $\beta(t)$  as time satisfies  $t < \tau_b \ll \tau_w$  (figure 5a–b). Besides, the subsequent stage is independent of the displacement-time

<sup>5</sup>For example, the first intense maximum of  $E_K$  occurs at  $t=0$  for the exponential case.

<sup>6</sup>Coupled in the same sense that velocity is coupled with position in a harmonic oscillator, i.e. with a  $90^\circ$  phase difference.

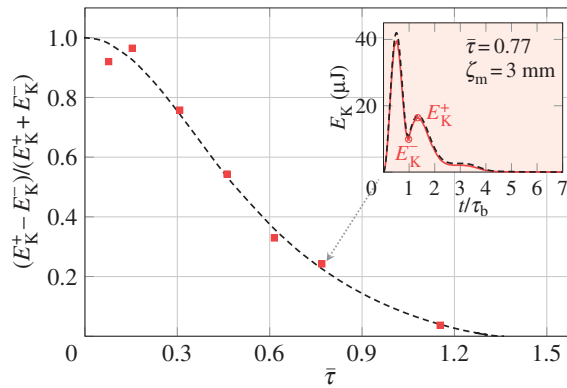


**Figure 4.** Inset: experimental (solid line) and theoretical (dashed line) kinetic energy  $E_K$  versus time.  $E_K^-$  is the local minimum of kinetic energy near  $t = \tau_b$  and  $E_K^+$  is the local maximum of kinetic energy due to the wave propagation. Experimental (squares) and theoretical (dashed line) contrast of kinetic energy versus  $\bar{\tau}$ . (Online version in colour.)

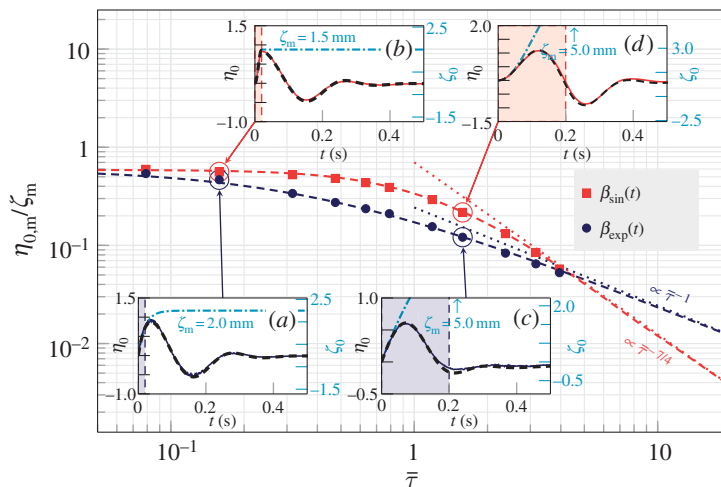


**Figure 5.** Insets: bottom and free-surface deformations in mm at  $r = 0$ ,  $\zeta_0$  and  $\eta_0$ , versus time ( $\zeta_0$  in dash-dotted lines;  $\eta_0$  experiments in solid lines; theory in dashed lines) for exponential (a,c) and half-sine (b,d) bottom displacements. The vertical dashed lines represent  $t = \tau_b$  for each run. The wave time scale  $\tau_w$  is found to be 130 ms in all the cases. Dimensionless free-surface maximal elevation at  $r = 0$ , against  $\bar{\tau}$  for different bottom displacements (see legend). Symbols are experimental data, dashed lines are theoretical results and dotted lines are asymptotic behaviours ( $\bar{\tau} \gg 1$ ). (Online version in colour.)

history of the bottom. Contrariwise, for  $\bar{\tau} \gtrsim 1$ , exponential and half-sine bed displacements induce free-surface responses that not only differ from rapid ones, but also from one another (figure 5c, d), e.g. the negative part of  $\eta_0$  is more pronounced for the half-sine case. This evidences that for  $\bar{\tau} \gtrsim 1$  the generated-wave shape depends on the nature of  $\beta(t)$  as well as on its typical time  $\tau_b$ , which confirms that the bottom kinematics is crucial in non-impulsive wave generation.

To understand more precisely its role, we plot in figure 5 the dimensionless maximal elevation of the free surface at  $r = 0$ ,  $\eta_{0,m}/\zeta_m$ , as a function of the time ratio  $\bar{\tau}$ . As expected,  $\eta_{0,m}$  decreases with  $\bar{\tau}$  and converges to the same asymptote for  $\bar{\tau} \ll 1$  independently of the nature of  $\beta(t)$ . For  $\bar{\tau} \gg 1$ , we observe two different behaviours:  $\eta_{0,m}$  decreases as  $\bar{\tau}^{-1}$  for exponential bottom displacements and as  $\bar{\tau}^{-7/4}$  for half-sine ones. This differs from one-dimensional experiments where a  $\bar{\tau}^{-1}$  power law fits both cases [29]. To summarize, when motion is transferred from the bottom to the free surface, the fluid layer behaves as a temporal high-pass filter (cut-off at  $\bar{\tau}^{-1} \approx 1$ ).

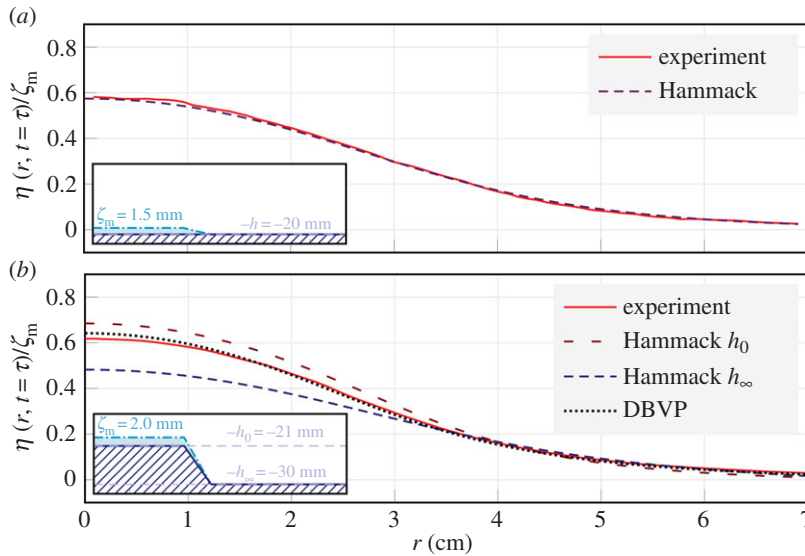


**Figure 6.** Insets: initial bottom shape  $\zeta(r, t = 0)$  (hatched areas), and final bottom shape after a half-sine impulsive deformation,  $\zeta(r, t \geq \tau = 20 \text{ ms})$  (coloured area/dash dotted lines) for: (a) *flat-bottom* initial configuration and (b) *non-flat-bottom* initial configuration: the piston is raised 9 mm above the basin bottom beforehand. Main: corresponding free surfaces at the end of the deformation,  $\eta(r, t = \tau)$ . (a) Experimental data (solid line); Hammack's linear theory (dashed line). (b) Experiments (solid line); Hammack's linear theory considering depth above the piston  $h_0 = 21 \text{ mm}$  (loosely dashed line); depth far from the piston,  $h_\infty = 30 \text{ mm}$ , (densely dashed line); decoupled boundary value problem (DBVP) approach (dotted line). See discussion in §3d. (Online version in colour.)

Note that  $\eta_{0,m}/\zeta_m$  does not reach unity when  $\bar{\tau} \rightarrow 0$ , as a consequence of the spatial low-pass filtering effects. The effects are highlighted in figure 6a, where we plot the spatial profiles of the bottom and the free surface at the end of an impulsive bed motion ( $t = \tau$ ;  $\bar{\tau} \ll 1$ ). We observe that the free surface is smoother than the bottom so the water column acts as a spatial low-pass filter. Note that this final free-surface profile is independent of  $\bar{\tau}$  and of the nature of  $\beta(t)$  (as long as  $\bar{\tau} \ll 1$ ). Low-pass filtering effects also explain why the dominant wavelength in our results,  $\lambda_w \approx 10 \text{ cm}$ , is larger than the size of the deformed region,  $2r_2 = 6.5 \text{ cm}$ .

### (c) Linear theory

The experimental data displayed in figures 4–6 are all found to be in good agreement with theoretical curves without any parameter fitting. The curves were calculated using the axisymmetric version of Hammack's tsunami-generation theory which neglects capillary, compressibility and viscous effects [38]. In our experiments, capillary effects are indeed negligible since the typical wavelength  $\lambda_w \approx 10 \text{ cm}$  is nearly 1 order of magnitude larger than the critical wavelength of capillary waves,  $\lambda_c = 2\pi\sqrt{\gamma/(\rho g)} \approx 1.4 \text{ cm}$  ( $\gamma \approx 50 \text{ dyn cm}^{-1}$  is the surface tension and  $\rho \approx 1 \text{ g cm}^{-3}$  the fluid density). The observed flow is also incompressible as  $\{\zeta_m/\tau_b, h/\tau_b, r_1/\tau_b\} \ll c_s$ , where  $c_s \approx 1500 \text{ m s}^{-1}$  is the sound speed in water [45]). Viscous effects are also absent as time scales associated with viscous processes,  $\tau_v \gtrsim 10 \text{ s}$ , are much larger than the experimental time scales.<sup>7</sup>

<sup>7</sup>Three different time scales, each of them associated with a different viscous process, can be calculated: (i) the decay time of the generated gravity waves due to the viscous boundary layer on the bottom:  $\tau_v^b = \tau_v \sinh 2k_w h \approx 50 \text{ s}$ , where  $\tau_v = \sqrt{\lambda_w^2 \tau_w / 2\pi^3 \nu}$  ( $\nu \approx 10^{-2} \text{ cm}^2 \text{ s}^{-1}$  is the kinematic viscosity), (ii) the wave decay time due to the viscous boundary layer on the free surface is  $\tau_v^s = 2\tau_v \tanh k_w h \approx 10 \text{ s}$ , and (iii) the viscous-diffusion characteristic time in the bulk  $\tau_v^b = \lambda_w^2 / 8\pi^2 \nu \approx 200 \text{ s}$  [46].



After neglecting capillary, compressibility and viscous effects, the flow can be assumed to be irrotational and hence the system can be expressed in terms of a velocity potential  $\phi$  that satisfies

$$\nabla^2 \phi = 0 \quad (3.1)$$

in the bulk. The experimental amplitude parameter  $\zeta_m/h$  is small enough to linearize boundary conditions [38]. Thus, if the bottom is initially flat, the dynamic condition at the free surface as well as the kinematic boundary conditions can be written as

$$\partial_t \phi|_{z=0} + g\eta = 0, \quad (3.2)$$

$$\partial_z \phi|_{z=-h} - \partial_t \zeta = 0 \quad (3.3)$$

and

$$\partial_z \phi|_{z=0} - \partial_t \eta = 0. \quad (3.4)$$

To solve this system of equations, we apply the Laplace transform in  $t$  to the displacement time function,  $\tilde{\beta}(s) \equiv \mathcal{L}\{\beta(t)\}(s)$ , and the Hankel transform of zeroth order in  $r$  to the spatial profile,  $\hat{\alpha}(k) \equiv \mathcal{H}_0\{\alpha(r)\}(k) \equiv \int_0^{+\infty} r J_0(kr) \alpha(r) dr$ , where  $J_0$  is the zeroth-order Bessel function of the first kind. The latter is equivalent to a two-dimensional (2D) Fourier transform under circular symmetry. Accordingly, the Hankel transform of the free-surface deformation may be written as [38]

$$\hat{\eta}(k, t) = \frac{\zeta_m \hat{\alpha}(k)}{\cosh kh} \cdot \mathcal{L}^{-1} \left\{ \frac{s^2 \tilde{\beta}(s)}{s^2 + \omega(k)^2} \right\} (k, t), \quad (3.5)$$

where  $\omega(k) = \sqrt{gk \tanh kh}$  is the gravity-wave dispersion relation. The direct and inverse Laplace transforms in equation (3.5) can be evaluated in closed form for both  $\beta_{\text{exp}}(t)$  and  $\beta_{\text{sin}}(t)$ . Besides, the spatial transform  $\hat{\alpha}(k)$  may be computed numerically. The spatio-temporal free-surface deformation  $\eta(r, t) = \mathcal{H}_0^{-1}\{\hat{\eta}(k, t)\}$  can be found likewise using a Fourier–Bessel series representation of  $\mathcal{H}_0^{-1}$  [47]. The velocity field can also be obtained by calculating the velocity potential  $\phi$  through the formula

$$\hat{\phi}(k, z, t) = \frac{\zeta_m \hat{\alpha}(k)}{\cosh kh} \cdot \mathcal{L}^{-1} \left\{ \frac{gs \tilde{\beta}(s)}{s^2 + \omega(k)^2} \left( \frac{s^2}{gk} \sinh kz - \cosh kz \right) \right\} (k, z, t). \quad (3.6)$$

Theoretical dashed lines in figures 4–6 are computed using equations (3.5) and (3.6) and display very good agreement with experimental data. The first factor in equation (3.5) is the Hankel transform of the final bottom deformation but modulated with a low-pass filter,  $(\cosh kh)^{-1}$ , that smooths the free surface as shown in figure 6. The second factor is spatio-temporal and relates the time  $t$  (corresponding to  $s$  in the Laplace domain) with the two characteristic times: the wave semi-period  $\tau_w$  (corresponding to  $\omega$ ) and the bottom rise time  $\tau_b$  (contained in  $\tilde{\beta}(s)$ ).

#### (d) Asymptotic analysis (decoupled boundary value problem approach)

In this section, we make an asymptotic analysis of (3.5) and (3.6), i.e. the linear model for tsunami-waves generation, for both the impulsive case ( $\bar{\tau} \ll 1$ ) and the creeping case ( $\bar{\tau} \gg 1$ ).

For the asymptotic expansion, consider first the impulsive limit  $\bar{\tau} \ll 1$ , so the expansion is made in terms of  $\bar{\tau}$ . We consider  $t \ll \tau_w$ ,  $s^2 + \omega^2 \sim s^2$ , the second factor of equation (3.5) becomes simply  $\beta(t)$  (and  $\partial_t \beta(t) \sinh kz/k$  in equation (3.6)), gravity effects vanish yielding interface elevations instantaneously equal to the bottom low-pass-filtered deformations

$$\eta(r, t) = \mathcal{H}_0^{-1} \left\{ \frac{\zeta_m \hat{\alpha}(k)}{\cosh kh} \right\} (r) \beta(t) + \mathcal{O}(\bar{\tau}^2) \quad (3.7)$$

and

$$\phi(r, z, t) = \mathcal{H}_0^{-1} \left\{ \frac{\zeta_m \hat{\alpha}(k) \sinh kz}{k \cosh kh} \right\} (r) \partial_t \beta(t) + \mathcal{O}(\bar{\tau}^2). \quad (3.8)$$

The asymptotic expansion is valid only for  $t \lesssim \tau_b$ . This is consistent with the behaviour observed experimentally at short times: the fluid and the free surface moves synchronously with the bottom

(figures 3*a* and 5 (insets)). For later times,  $t \gtrsim \tau_b$ ,  $\beta(t)$  can be considered as a Heaviside function  $H(t)$  provided that  $\bar{\tau} \ll 1$ . Hence,  $\tilde{\beta}(s) = \tilde{H}(s) = s^{-1}$ , and the second factor in equation (3.5) becomes a propagation term:  $\hat{\eta}(k, t) = \zeta_m \hat{\omega}(k) \cos \omega(k)t / \cosh kh$ . As stated by Kajiwara [28], this is equivalent to a Cauchy–Poisson wave problem in which only the final bottom deformation is low-pass filtered and transferred to the surface as an initial condition. Likewise, we have shown that the fluid is motionless when the bottom motion ends. No trace from the temporal features of the initial motion is left. This explains the memory loss of the bottom-displacement history observed in our experiments.

Like free-surface deformation, velocity potential for the impulsive limit ( $\bar{\tau} \ll 1$ ) has a striking feature: gravity plays no role during the bottom motion, i.e.  $t \leq \tau_b \ll \tau_w$  (equations (3.5) and (3.6)). Accordingly, we analyse the limit  $g \rightarrow 0$ . At leading order, we can drop the gravity term in equation (3.2), so  $\phi|_{z=0} = 0$  and the free surface  $\eta$  decouples from equations (3.1)–(3.3). This yields a decoupled boundary value problem (DBVP) for the velocity potential  $\phi$ , equivalent to solve Laplace equation with given boundary conditions:

$$\nabla^2 \phi = 0, \quad \phi|_{z=0} = 0 \quad \text{and} \quad \partial_z \phi|_{z=-h} = \partial_t \zeta. \quad (3.9)$$

The free-surface deformation  $\eta$  may then be obtained from equation (3.4). Note that for any bed motion  $\zeta(x, y, t)$  separable in space and time, i.e.  $\zeta(x, y, t) = \zeta_m \alpha(x, y) \beta(t)$ , the velocity field generated by (3.9) scales with the velocity of the bottom,  $\partial_t \beta$ , while the streamlines and vector orientation are steady. The boundary condition  $\phi|_{z=0} = 0$  is consistent with the experimentally observed features in figure 3*a*: a vertical velocity field at the free surface.

Another interesting limit stands for the creeping case where  $\bar{\tau} \gg 1$ . Accordingly, the expansion now given in terms of  $\bar{\tau}^{-1}$ . We consider  $t \gg \tau_w$ , the free-surface deformation from (3.5) and the velocity field from (3.6) yield at dominant order to

$$\eta(r, t) = \mathcal{H}_0^{-1} \left\{ \frac{\zeta_m \hat{\omega}(k)}{gk \sinh kh} \right\} (r) \partial_{tt} \beta(t) + \mathcal{O}(\bar{\tau}^{-4}) \quad (3.10)$$

and

$$\phi(r, z, t) = \mathcal{H}_0^{-1} \left\{ -\frac{\zeta_m \hat{\omega}(k) \cosh kz}{k \sinh kh} \right\} (r) \partial_t \beta(t) + \mathcal{O}(\bar{\tau}^{-2}). \quad (3.11)$$

Again, the velocity potential is independent of  $g$ . Although, the dependence on  $k$  is different than in the impulsive case. Note that the free-surface-deformation dominant term is not  $\mathcal{O}(1)$ , which is equal to zero, but the following one, which is  $\mathcal{O}(\bar{\tau}^{-2})$ . The term is proportional to the ratio of the bottom acceleration and gravity.<sup>8</sup> Be aware that there is not any conflict between the form of the asymptotic expansions and the asymptotic behaviour of  $\eta_{0,m}/\zeta_m$  in the creeping limit ( $\bar{\tau} \gg 1$ ) depicted in figure 5. For our largest values of  $\bar{\tau}$ , maximal deformations are attained at  $t \gtrsim \tau_w$ , for which the asymptotic expansion is not valid.

Another DBVP can be found for this case. Consider  $g \rightarrow \infty$  in equation (3.2): hence  $\eta = 0$ . The new DBVP is again equivalent to solve Laplace equation but with a different boundary condition at  $z = 0$

$$\nabla^2 \phi = 0, \quad \partial_z \phi|_{z=0} = 0 \quad \text{and} \quad \partial_z \phi|_{z=-h} = \partial_t \zeta. \quad (3.12)$$

The properties are similar to those of the impulsive case: proportionality to  $\partial_t \beta$  and steady streamlines for space–time separable functions. We find again in  $\partial_z \phi|_{z=0} = 0$  that the velocity field is horizontal at the free surface as observed experimentally in figure 3*c*.

For both limits,  $\bar{\tau} \gg 1$  and  $\bar{\tau} \ll 1$ , the DBVP can be straightforwardly solved using a finite-difference scheme for the Laplace equation [48, pp. 1024–1031]. The method differs from Green's function approach developed in [43]. The computed streamlines fit in an excellent way the measured velocity field (figure 3*a,c*). On the other hand, while for  $\bar{\tau} \gg 1$ ,  $\eta \simeq 0$ , for initially flat bottoms undergoing impulsive uplifts ( $\bar{\tau} \ll 1$ ),  $\eta$  can be obtained from equation (3.4). This leads to the spatial low-pass filtered results found previously.

<sup>8</sup>The asymptotic expansion goes as  $\tau^{-2n}$  as a consequence of the term  $s^2/(s^2 + \omega^2)$  inside the inverse Laplace transform in equation (3.5).

The DBVP approach has another great advantage: it can be adapted to initially arbitrary-shaped-bottom basins by simply writing the bottom condition as  $\partial_z \phi|_{z=-h(x,y)} = \partial_t \zeta$ . To experimentally validate the DBVP approach under this configuration, we considered a non-flat-bottom initial condition in our tank, i.e. the piston was raised above the basin-bottom level beforehand (figure 6*b* (inset)). In figure 6*b*, we plot the spatial profile of the free surface at the end of an impulsive bottom deformation ( $\bar{\tau} \ll 1$ ). We observe that the DBVP results displays very good agreement with the experimental profile. Comparison with other initially flat-bottom models is not straightforward: for instance, the water depth  $h$  used in Hammack's linear theory is not defined anymore. Two different water depths are involved:  $h_0$  above the piston and  $h_\infty$  elsewhere. The spatial profiles obtained with Hammack's linear theory, using either  $h = h_0$  or  $h = h_\infty$ , are significantly different from the experimental profile. This demonstrates the usefulness of the DBVP approach for taking into account varying bathymetry, if present (see the discussion below).

Note that dependence on time in the DBVP equations is slaved to  $\zeta(t)$ . Thus, to compute free-surface deformation during an impulsive bottom motion ( $\bar{\tau} \ll 1$ ,  $t \leq \tau_b$ ), Laplace equations need to be solved just once and then scaled by  $\beta(t)$ . For later times ( $t > \tau_b$ ), classical wave-propagation routines can be easily plugged. The initial waveform will be provided by the impulsive DBVP at the end of the bottom motion (static initial condition).

Owing to its low cost, one solving-Laplace-equation step, the method may be used as a computationally affordable routine to incorporate terrain conditions in impulsive tsunami generation real scenarios.

## (e) Application to tsunamis

Tsunami-generation experiments in laboratory tanks deal with a clear compromise between scalability to realistic scenarios and feasibility, controllability and measurability. The aim of our experiments was to understand the role of the spatio-temporal features of bottom motion on induced waves (e.g. measuring simultaneously the velocity field and the free-surface deformation during the process). Thus, we had to make a suitable choice of the dimensions of the experiments. Accordingly, our experimental parameters ( $\zeta_m^+/h^+ = 0.06 - 0.2$ ,  $r_1^+/h^+ = 1$ ,  $\tau_b^+ = 10 - 500$  ms) obviously differ from those of real tsunamis ( $\zeta_m^*/h^* \sim 10^{-3}$ ,  $r_1^*/h^* \sim 10 - 20$ ,  $\tau_b^* \sim 1 - 100$  s) by several orders of magnitude. Notwithstanding, we have shown that at our chosen scales, bottom-induced wave generation is governed by Hammack's linear theory, and in its fast and slow asymptotics, by the DBVP framework. In this section, we carefully check the validity of the same theoretical frameworks when scaled up to typical tsunami scales. The check-up requires not only the analysis of the linear-theory assumptions but also the evaluation of some key dimensionless numbers.

- Concerning viscosity and capillarity effects, we can verify that both effects decrease as length scales increases. This means that in real scenarios, they should be even smaller than in our set-up.<sup>9</sup>
- Nonlinear effects are measurable through the dimensionless quantity  $\zeta_m/h$ , which is much lower in real-tsunami scenarios than in our experiments ( $\zeta_m^*/h^* \sim 10^{-3} \ll \zeta_m^+/h^+ \sim 10^{-1}$ ). This means that for real-tsunami scenarios linear theory should fit even better.<sup>10</sup>
- Geometry issues, which can be quantified by the size ratio  $r_1/h$ , require a deeper analysis. In our experiments, we fixed  $r_1^+/h^+ = 1$  to highlight the spatial low-pass filtering. For accepted tsunami values ( $r_1^*/h^* \sim 10 - 20$ ), filtering effects are expected to be weak. However, recent and more direct evidence shows that tsunami initial waveforms have a

<sup>9</sup>Compressibility, on the other hand, may have some effect as  $h/\tau_b$  and  $r_1/\tau_b$  become non-negligible compared with the speed of sound  $c_s$  at plausible tsunami scenarios. However, it is far from being dominant. Numerical integrations show that acoustic-gravity waves just superpose on a main signal which is equal to incompressible gravity wave (see e.g. fig. 2 in [45]).

<sup>10</sup>Since,  $\eta/\zeta_m$  and  $\phi/\zeta_m$  are independent of  $\zeta_m$  (see equations (3.5) and (3.6)), as a consequence of linearity, our experiments are able to capture the dynamic features for smaller amplitude waves, as those from real-tsunami scenarios.

complex spatial distribution with significantly smaller length scales:  $r_1^*/h^* \lesssim 5$ , as shown with data from two recent tsunami sources (including the large 2011 Tohoku tsunami in Japan) [49,50]. Their spatial distributions may be approximated by spherical-cap deformations, which yield low-pass filtering  $\eta_{0,m}^*/\zeta_m^*$ -corrections of 10% [28].

- Dynamic effects, can be analysed in terms of the time ratio  $\bar{\tau} = \tau_b/\tau_w$ . In this case, the typical tsunami range of time ratios  $\bar{\tau}^* \in [0.003, 0.3]$  is located on the left-hand side of figure 5, which makes them suitable for the impulsive DBVP approach. In our experiments,  $\bar{\tau}^\dagger \in [0.08, 4]$ . First, notice that although the fastest tsunamis are beyond our experimental range, the asymptote for  $\bar{\tau} \ll 1$  is largely attained within it, so that our work covers faster tsunamigenic earthquakes. Besides, temporal high-pass filtering effects become significant for slowest tsunami scenarios. For instance, the 2004 Sumatra-Andaman tsunamigenic earthquake in Indonesia displayed rise times estimated at  $\tau_b^* \approx 3$  min while  $\tau_w^* \approx 10$  min (i.e.  $\bar{\tau}^* \sim 0.3$ ) [51]. According to our results, this yields  $\eta_{0,m}/\zeta_m$ -corrections from 10% (half-sine displacement time function) to 40% (exponential rise) compared to the nearly instantaneous case. Furthermore, as earthquakes may involve different timescales between rise and subsidence times, our extended range of  $\bar{\tau}^\dagger$ -values is of importance to know from which timescales surface waves generated by a bottom motion become negligible.<sup>11</sup>
- Effects due to bathymetry (non-flat bottoms initial conditions) are hard to quantify by a single dimensionless parameter, since corrections will depend on the particular geometrical features around the source. However, it is known that water depth may vary abruptly in the fault crosswise direction in subduction zones, the archetype of tsunamigenic regions. To illustrate with one case, water depth varies by a factor of 3 over 60 km at the source of the 2011 Tohoku tsunami [52]. Although the source bathymetry of this event is far from being axisymmetric, the initial condition is roughly comparable to figure 6*b*. Finally, we have shown that the DBVP approach that we provide in this study may be applied to uncover bathymetry effects on tsunami waveforms.

Note that the application of some of our results to real-time tsunami forecasts may be limited by the fact that seismic data do not provide much details about the seabed kinematics (e.g. rise time, spatial resolution). For instance, the currently used spatial resolution for bottom deformations at tsunami sources is  $25 \times 50 \text{ km}^2$  (NOAA SIFT Green's functions). However, higher spatial resolutions in tsunami sources may become available soon in standard real-time simulations. Indeed, Crowell *et al.* [53] have recently shown that it is possible to obtain seabed deformations at high resolutions within 2 min after the strike of an earthquake using GPS data.

## 4. Conclusion

In conclusion, we have investigated the generation of free surface waves by an underwater moving bottom. The experiments, which included simultaneous measurements of fluid velocity field and free-surface displacement in an initially flat-bottom configuration, display excellent agreement without any parameter fitting with a linear theory of gravity waves. Although the small scale of our wave-generation set-up cannot be compared to real-tsunami scenarios, our experiments are able to capture underlying features of dynamic coupling in tsunami-wave generation. Essentially, the fluid layer transfers motion from the bottom to the free surface as a temporal high-pass filter coupled with a spatial low-pass filter. Transfer models that perform a simple translation, such as those used by tsunami warning systems, overlook both filters effects. Supported on measured velocity fields, we have developed an alternative theoretical guideline for taking into account spatial filtering for impulsive bottom uplifts. Furthermore, the impulsive

<sup>11</sup> However, linear-theory corrections due to 'uprise slowness' yield lower amplitudes, while those of the observed tsunami were larger. The cause may be a resonance mechanism due to a richer bottom kinematics, e.g. a slowly spreading fault, as predicted in [15]. To analyse this, we are running experiments on a new setup that supports complex-dynamics scenarios. Results are far from the scope of this manuscript and will be published separately.

model was adapted to predict the initial waveforms generated for initially non-flat-bottom configurations. This is achieved via a one-step-in-time numerical integration of Laplace equation in a suitable domain and under given boundary conditions. The results have been successfully validated with experiments. The new guideline may help to include *in situ* bathymetry data in tsunami scenarios at low computational cost: this would be a key for improving real-time forecast tsunami simulations.

Further experimental work will involve studying other spatial/dynamic features of realistic tsunami scenarios, e.g. non-axisymmetric spatial distribution, complex bottom kinematics (e.g. spreading faults). Beyond tsunami-oriented experiments, we also intend to probe nonlinear effects for larger bottom deformations. Further theoretical work, will include a rigorous higher order analysis of the asymptotic expansions for the impulsive and creeping limits.

**Data Accessibility.** All the data used throughout this article are available at a public repository: <http://dx.doi.org/10.6084/m9.figshare.979238>.

**Authors' Contributions.** T.J. performed the experiments, set up the mechanical excitation control, analysed and interpreted data, adapted the linear model and wrote the paper; L.G. performed the experiments, wrote data processing codes (PIV and free-surface detection), analysed and interpreted data, developed the DBVP approach and wrote the paper. T.J. and L.G. contributed equally to this work. G.R.-C. performed the experiments; M.B. conceived and designed the study; E.F. conceived, designed and coordinated the study. All the authors discussed and edited the manuscript and gave final approval for publication.

**Competing Interests.** We declare we have no competing interests.

**Funding.** T.J. was supported by the DGA-CNRS PhD program and L.G. by a 2012 Postdoctoral Fellowship of the AXA Research Fund. G.R.-C. was supported by the program Research in Paris 2011 of the City of Paris. This research was financed by the ANR Turbulon 12-BS04-0005.

**Acknowledgements.** We acknowledge F. Dias for fruitful discussions about this topic. We thank A. Lantheaume and the LIED (Université Paris Diderot) for their technical help.

## References

1. Mungov G, Eblé M, Bouchard R. 2013 DART<sup>®</sup> tsunameter retrospective and real-time data: a reflection on 10 years of processing in support of tsunami research and operations. *Pure Appl. Geophys.* **170**, 1369–1384. (doi:10.1007/s00024-012-0477-5)
2. Okada Y. 1985 Surface deformation due to shear and tensile faults in a half-space. *Bull. Seismol. Soc. Am.* **75**, 1135–1154.
3. Arcas D, Uslu B. 2010 PMEL tsunami forecast series: vol. 2. Technical report.
4. Geist EL, Titov VV, Synolakis C. 2006 Tsunami: WAVE of CHANGE. *Sci. Am.* **294**, 56–63. (doi:10.1038/scientificamerican0106-56)
5. Geist EL, Bilek SL, Arcas D, Titov VV. 2006 Differences in tsunami generation between the December 26, 2004 and March 28, 2005 Sumatra earthquakes. *Earth Planets Space* **58**, 185–193. (doi:10.1186/BF03353377)
6. Maeda T, Furumura T, Sakai S, Shinohara M. 2011 Significant tsunami observed at ocean-bottom pressure gauges during the 2011 off the Pacific coast of Tohoku Earthquake. *Earth Planets Space* **63**, 803–808. (doi:10.5047/eps.2011.06.005)
7. Tanioka Y, Seno T. 2001 Sediment effect on tsunami generation of the 1896 Sanriku Tsunami Earthquake. *Geophys. Res. Lett.* **28**, 3389–3392. (doi:10.1029/2001GL013149)
8. Dutykh D, Dias F. 2010 Influence of sedimentary layering on tsunami generation. *Comput. Methods Appl. Mech. Eng.* **199**, 1268–1275. (doi:10.1016/j.cma.2009.07.011)
9. Synolakis C, Bardet JP, Borrero JC, Davies HL, Okal EA, Silver EA, Sweet S, Tappin DR. 2002 The slump origin of the 1998 Papua New Guinea Tsunami. *Proc. R. Soc. Lond. A* **458**, 763–789. (doi:10.1098/rspa.2001.0915)
10. Okal EA, Synolakis C. 2004 Source discriminants for near-field tsunamis. *Geophys. J. Int.* **158**, 899–912. (doi:10.1111/j.1365-246X.2004.02347.x)
11. Sammarco P, Renzi E. 2008 Landslide tsunamis propagating along a plane beach. *J. Fluid Mech.* **598**, 107–119. (doi:10.1017/S0022112007009731)
12. Geist EL, Titov VV, Arcas D, Pollitz FF, Bilek SL. 2007 Implications of the 26 December 2004 Sumatra-Andaman Earthquake on tsunami forecast and assessment models for great Subduction-Zone Earthquakes. *Bull. Seismol. Soc. Am.* **97**, S249–S270. (doi:10.1785/0120050619)



13. Synolakis C, Liu P, Carrier G, Yeh H. 1997 Tsunamigenic sea-floor deformations. *Science* **278**, 598–600. (doi:10.1126/science.278.5338.598)
14. Geist EL. 1998 Local tsunamis and earthquake source parameters. *Adv. Geophys.* **39**, 117–209. (doi:10.1016/S0065-2687(08)60276-9)
15. Todorovska MI, Trifunac MD. 2001 Generation of tsunamis by a slowly spreading uplift of the sea floor. *Soil Dyn. Earthquake Eng.* **21**, 151–167. (doi:10.1016/S0267-7261(00)00096-8)
16. Kanamori H. 1972 Mechanism of tsunami earthquakes. *Phys. Earth Planet. Interiors* **6**, 346–359. (doi:10.1016/0031-9201(72)90058-1)
17. Titov VV, Gonzalez FI 1997 Implementation and testing of the method of splitting tsunami (MOST) model. Technical Report NOAA Technical Memorandum ERL PMEL-112, Seattle.
18. UNESCO. 1997 IUGG/IOC Time Project: numerical method of tsunami simulation with the leap-frog scheme. Technical Report IOC Manuals and Guides No. 35, Paris.
19. Ichiye T. 1958 A theory on the generation of tsunamis by an impulse at the sea bottom. *J. Oceanogr. Soc. Jpn* **14**, 41–44.
20. Fuhrman DR, Madsen PA. 2009 Coastal engineering. *Coastal Eng.* **56**, 747–758. (doi:10.1016/j.coastaleng.2009.02.004)
21. Grilli ST, Vogelmann S, Watts P. 2002 Development of a 3D numerical wave tank for modeling tsunami generation by underwater landslides. *Eng. Anal. Boundary Elements* **26**, 301–313. (doi:10.1016/S0955-7997(01)00113-8)
22. Grilli ST, Dias F, Guyenne P, Fochesato C, Enet F. 2010 Progress in fully nonlinear potential flow modeling of 3D extreme ocean waves. *Adv. Numer. Simul. Nonlinear Water Wave (Advances in Coastal and Ocean Engineering)*, Q. Ma, ed **11**, 75–128.
23. Gisler GR. 2008 Tsunami simulations. *Annu. Rev. Fluid Mech.* **40**, 71–90. (doi:10.1146/annurev.fluid.40.111406.102208)
24. Kakinuma T 2009 Numerical simulation of tsunami generation. *Kôkyûroku* **1645**, 14–21. (<http://hdl.handle.net/2433/140682>)
25. Kervella Y, Dutykh D, Dias F. 2007 Comparison between three-dimensional linear and nonlinear tsunami generation models. *Theor. Comput. Fluid Dyn.* **21**, 245–269. (doi:10.1007/s00162-007-0047-0)
26. Ma G, Shi F, Kirby JT. 2012 Shock-capturing non-hydrostatic model for fully dispersive surface wave processes. *Ocean Model.* **43–44**, 22–35. (doi:10.1016/j.ocemod.2011.12.002)
27. Grilli ST, Harris JC, Tajalli Bakhsh TS, Masterlark TL, Kyriakopoulos C, Kirby JT, Shi F. 2012 Numerical simulation of the 2011 Tohoku tsunami based on a new transient FEM co-seismic source: comparison to far- and near-field observations. *Pure Appl. Geophys.* **170**, 1333–1359. (doi:10.1007/s00024-012-0528-y)
28. Kajiura K. 1963 The leading wave of a tsunami. *Bull. Earthquake Res. Inst.* **41**, 535–571.
29. Hammack JL. 1973 A note on tsunamis: their generation and propagation in an ocean of uniform depth. *J. Fluid Mech.* **60**, 769–799. (doi:10.1017/S00222112073000479)
30. Dutykh D, Dias F, Kervella Y. 2006 Linear theory of wave generation by a moving bottom. *Comptes Rendus de l'Académie des Sciences Serie I-Mathématique* **343**, 499–504. (doi:10.1016/j.crma.2006.09.016)
31. Takahasi R, Hatori T. 1962 A model experiment on the Tsunami generation from a bottom deformation area of elliptic shape. *Bull. Earthquake Res. Inst.* **40**, 873–883.
32. Wiegel RL. 1955 Laboratory studies of gravity waves generated by the movement of a submerged body. *Trans. Am. Geophys. Union* **36**, 759–774. (doi:10.1029/TR036i005p00759)
33. Enet F, Grilli ST. 2007 Experimental study of tsunami generation by three-dimensional rigid underwater landslides. *J. Waterway Port Coastal Ocean Eng.* **133**, 442–454. (doi:10.1061/(ASCE)0733-950X(2007)133:6(442))
34. Fritz HM, Hager WH, Minor HE. 2003 Landslide generated impulse waves. 1. Instantaneous flow fields. *Exp. Fluids* **35**, 505–519. (doi:10.1007/s00348-003-0659-0)
35. Fritz HM, Hager WH, Minor HE. 2003 Landslide generated impulse waves. 2. Hydrodynamic impact craters. *Exp. Fluids* **35**, 520–532. (doi:10.1007/s00348-003-0660-7)
36. Viroulet S, Sauret A, Kimmoun O. 2014 Tsunami generated by a granular collapse down a rough inclined plane. *Europhys. Lett.* **105**, 34004. (doi:10.1209/0295-5075/105/34004)
37. Enet F, Grilli ST, Watts P 2003 Laboratory experiments for tsunamis generated by underwater landslides: Comparison with numerical modeling. In *Proc. Thirteenth (2003) International Offshore and Polar Engineering Conference*, pp. 372–379.
38. Hammack JL 1972 *Tsunamis—a model of their generation and propagation*. PhD thesis, California Institute of Technology—W. M. Keck Laboratory of Hydraulics and Water Resources, Pasadena, CA, USA.

39. Sanchis A, Jensen A. 2011 Dynamic masking of PIV images using the Radon transform in free surface flows. *Exp. Fluids* **51**, 871–880. (doi:10.1007/s00348-011-1101-7)
40. Westerweel J, Dabiri D, Gharib M. 1997 The effect of a discrete window offset on the accuracy of cross-correlation analysis of digital PIV recordings. *Exp. Fluids* **23**, 20–28. (doi:10.1007/s003480050082)
41. Meinhart CD, Wereley S, Santiago J. 2000 A PIV algorithm for estimating time-averaged velocity fields. *J. Fluids Eng.* **122**, 285–289. (doi:10.1115/1.483256)
42. Gordillo L, Jamin T, Ruiz-Chavarría G, Berhanu M, Falcon E. 2014 Experiments on tsunami waves. figshare. (doi:10.6084/m9.figshare.979238)
43. Tyvand PA, Storhaug ARF. 2000 Green functions for impulsive free-surface flows due to bottom deflections in two-dimensional topographies. *Phys. Fluids* **12**, 2819–2833. (doi:10.1063/1.1290392)
44. Dutykh D, Dias F. 2009 Energy of tsunami waves generated by bottom motion. *Proc. R. Soc. A* **465**, 725–744. (doi:10.1098/rspa.2008.0332)
45. Nosov MA. 1999 Tsunami generation in compressible ocean. *Phys. Chem. Earth Part B* **24**, 437–441. (doi:10.1016/S1464-1909(99)00025-8)
46. Miles JW. 1967 Surface-wave damping in closed basins. *Proc. R. Soc. Lond. A* **297**, 459–475. (doi:10.1098/rspa.1967.0081)
47. Arfken GB, Weber HJ. 2005 *Mathematical methods for physicists*, 6th edn. Oxford, UK: Elsevier Academic Press.
48. Press WH, Teukolsky SA, Vetterling WT, Flannery BP. 2007 *Numerical recipes 3rd edition: the art of scientific computing*, 3rd edn. New York, NY, USA: Cambridge University Press.
49. Fujii Y, Satake K. 2008 Tsunami waveform inversion of the 2007 Bengkulu, southern Sumatra, earthquake. *Earth Planets Space* **60**, 993–998. (doi:10.1186/BF03352856)
50. Fujii Y, Satake K, Sakai S, Shinohara M, Kanazawa T. 2011 Tsunami source of the 2011 off the Pacific coast of Tohoku Earthquake. *Earth Planets Space* **63**, 815–820. (doi:10.5047/eps.2011.06.010)
51. Fujii Y, Satake K. 2007 Tsunami Source of the 2004 Sumatra-Andaman Earthquake Inferred from Tide Gauge and Satellite Data. *Bull. Seismol. Soc. Am.* **97**, S192–S207. (doi:10.1785/0120050613)
52. Oguri K, Kawamura K, Sakaguchi A, Toyofuku T, Kasaya T, Murayama M, Fujikura K, Glud RN, Kitazato H. 2013 Hadal disturbance in the Japan Trench induced by the 2011 Tohoku–Oki Earthquake. *Sci. Rep.* **3**, 1915.
53. Crowell BW, Bock Y, Melgar D. 2012 Real-time inversion of GPS data for finite fault modeling and rapid hazard assessment. *Geophys. Res. Lett.* **39**, L09305.